



















In the format provided by the authors and unedited.

First light demonstration of the integrated superconducting spectrometer

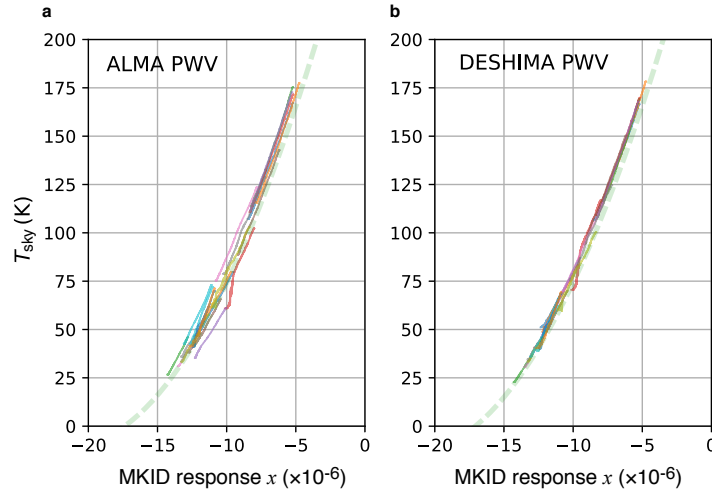
Akira Endo ^{1,2*}, Kenichi Karatsu^{1,3}, Yoichi Tamura ⁴, Tai Oshima^{5,6}, Akio Taniguchi ⁴, Tatsuya Takekoshi ^{7,8}, Shin'ichiro Asayama⁵, Tom J. L. C. Bakx ^{4,5,9}, Sjoerd Bosma ¹, Juan Bueno³, Kah Wuy Chin^{5,10}, Yasunori Fujii⁵, Kazuyuki Fujita¹¹, Robert Huiting³, Soh Ikarashi¹, Tsuyoshi Ishida⁷, Shun Ishii ^{5,12}, Ryohei Kawabe ^{5,6,10}, Teun M. Klapwijk ^{2,13}, Kotaro Kohno ^{7,14}, Akira Kouchi¹¹, Nuria Llombart¹, Jun Maekawa⁵, Vignesh Murugesan³, Shunichi Nakatsubo¹⁵, Masato Naruse¹⁶, Kazushige Ohtawara ⁵, Alejandro Pascual Laguna ^{1,3}, Junya Suzuki ¹⁷, Koyo Suzuki⁴, David J. Thoen ^{1,2}, Takashi Tsukagoshi⁵, Tetsutaro Ueda⁴, Pieter J. de Visser ³, Paul P. van der Werf ¹⁸, Stephen J. C. Yates¹⁹, Yuki Yoshimura ⁷, Ozan Yurduseven¹ and Jochem J. A. Baselmans ^{1,3}

¹Faculty of Electrical Engineering, Mathematics and Computer Science, Delft University of Technology, Delft, The Netherlands. ²Kavli Institute of NanoScience, Faculty of Applied Sciences, Delft University of Technology, Delft, The Netherlands. ³SRON—Netherlands Institute for Space Research, Utrecht, The Netherlands. ⁴Division of Particle and Astrophysical Science, Graduate School of Science, Nagoya University, Nagoya, Japan. ⁵National Astronomical Observatory of Japan, Mitaka, Japan. ⁶The Graduate University for Advanced Studies (SOKENDAI), Mitaka, Japan. ⁷Institute of Astronomy, Graduate School of Science, The University of Tokyo, Mitaka, Japan. ⁸Graduate School of Informatics and Engineering, The University of Electro-Communications, Chofu, Japan. ⁹School of Physics & Astronomy, Cardiff University, Cardiff, UK. ¹⁰Department of Astronomy, School of Science, University of Tokyo, Tokyo, Japan. ¹¹Institute of Low Temperature Science, Hokkaido University, Sapporo, Japan. ¹²Joint ALMA Observatory, Santiago, Chile. ¹³Physics Department, Moscow State Pedagogical University, Moscow, Russia. ¹⁴Research Center for the Early Universe, Graduate School of Science, The University of Tokyo, Tokyo, Japan. ¹⁵Institute of Space and Astronautical Science, Japan Aerospace Exploration Agency, Sagami-hara, Japan. ¹⁶Graduate School of Science and Engineering, Saitama University, Saitama, Japan. ¹⁷High Energy Accelerator Research Organization (KEK), Tsukuba, Japan. ¹⁸Leiden Observatory, Leiden University, Leiden, The Netherlands. ¹⁹SRON—Netherlands Institute for Space Research, Groningen, The Netherlands. *e-mail: a.endo@tudelft.nl

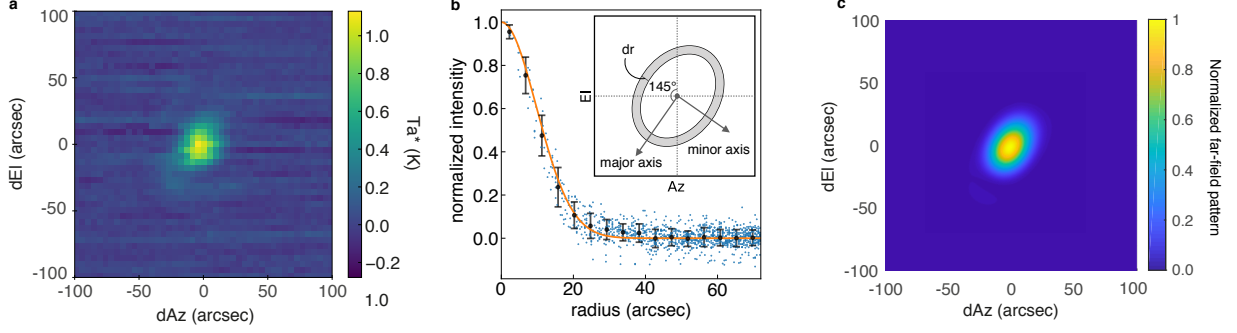
Supplementary Information For:

First light demonstration of the integrated superconducting spectrometer

Akira Endo, Kenichi Karatsu, Yoichi Tamura, Tai Oshima, Akio Taniguchi, Tatsuya Takekoshi, Shinichiro Asayama, Tom J.L.C. Bakx, Sjoerd Bosma, Juan Bueno, Kah Wuy Chin, Yasunori Fujii, Kazuyuki Fujita, Robert Huiting, Soh Ikarashi, Tsuyoshi Ishida, Shun Ishii, Ryohei Kawabe, Teun M. Klapwijk, Kotaro Kohno, Akira Kouchi, Nuria Llombart, Jun Maekawa, Vignesh Murgesan, Shunichi Nakatsubo, Masato Naruse, Kazushige Ohtawara, Alejandro Pascual Laguna, Junya Suzuki, Koyo Suzuki, David J. Thoen, Takashi Tsukagoshi, Tetsutaro Ueda, Pieter J. de Visser, Paul P. van der Werf, Stephen J.C. Yates, Yuki Yoshimura, Ozan Yurduseven, and Jochem J.A. Baselmans



Supplementary Fig. S1. Conversion from the relative MKID frequency response x to sky brightness temperature T_{sky} . **a**, Sky temperature T_{sky} as a function of relative MKID frequency shift x for a representative filterbank channel. x is defined relative to when an ambient temperature black body is loading the beam coming out of the cryostat: $x \equiv \{f(T_{\text{sky}}) - f(T_{\text{amb}})\}/f(T_{\text{amb}})$. The analysis is based on time-dependent PWV values taken directly from the ALMA radiometer³¹ without any correction. Each solid curve is taken with one skydip measurement. The dashed curve is a square-law fit to all measurements. **b**, Improved calibration model, after an iterative parameter fit which takes the PWV as a fitting parameter that is common to all filterbank channels.



Supplementary Fig. S2. The beam pattern of ASTE/DESHIMA. **a**, The DESHIMA 350 GHz image of Mars. The response of all spectral channels are added together. The color scale represents antenna temperature. **b**, The radial profile of the 350 GHz image of Mars with an apparent diameter of $3.99''$. Since the beam shape is elliptical, the normalized intensities (blue dots) are measured with elliptical annuli as a function of their minor radii. The radius of each pixel in the image is defined as minor axis of an ellipse (corresponding to the beam shape of panel a) which crosses it, and the blue data points indicate the normalized intensities at each pixel in the image. The black points and error bars show the mean and standard deviation of the normalized intensity at a radial bin in steps of $dr = 4.5''$ (inset). After correcting for the ellipticity, the main beam is well described by a Gaussian with a FWHM of 22.8 ± 3.1 arcseconds (orange line). **c**, Normalized far-field beam pattern, simulated assuming a 4° offset from the ideal optical axis at the lens-antenna on chip.

Supplementary Note 1. MAIN BEAM SIZE AND EFFICIENCY

We measure the main-beam shape and efficiency on a Mars image where Mars cannot be considered as a point source (i.e., $\Omega_{\text{source}} \ll \Omega_{\text{MB}}$, where the former and latter are the solid angles of the source and the main beam, respectively). The Mars image is produced by putting time-stream data, which are already flux-calibrated by the standard chopper-wheel method, into 2-dimensional pixels (Supplementary Fig. S2a). Then we fit a 2-dimensional Gaussian to this continuum map to measure the intrinsic beam size and amplitude. We obtain a peak antenna temperature of $T_a^* = 1.06 \pm 0.1$ K and the half-power beam width (HPBW) of $31.4'' \pm 2.8''$ by $22.8'' \pm 3.1''$ with a position angle of 145 degrees. The beam radial profile is presented in Supplementary Fig. S2b. The antenna temperature is related to the main beam efficiency as the equation

$$T_a^* = \frac{\int_{\text{source}} P_n(\theta, \phi) d\Omega}{\int_{4\pi} P_n(\theta, \phi) d\Omega} T_{\text{brightness}} = \eta_{\text{MB}} \frac{\Omega_{\text{source}}}{\Omega_{\text{MB}}} T_{\text{brightness}}, \quad (\text{S1})$$

where P_n is the power pattern, Ω_{MB} and Ω_{source} are the solid angle of main beam and the source, respectively, and η_{MB} is the main beam efficiency. The solid angle of an elliptical

main beam is expressed as $\Omega_{\text{MB}} = \frac{\pi\theta_{\text{major}}\theta_{\text{minor}}}{4\ln 2}$, where θ_{major} and θ_{minor} are the FWHMs of the main beam measured along the major and minor axes, respectively. We regard the brightness distribution of Mars as a disk with a uniform intensity of $T_{\text{brightness}} = 210$ K and an apparent diameter of $3.99''$, and obtain $\eta_{\text{MB}} = 0.34 \pm 0.03$ at 350 GHz.

Supplementary Note 2. JACK-KNIFE ESTIMATION OF THE NOISE LEVEL

Since each MKID is an independent detector, the noise level of each ISS channel is determined by applying an iterative integration method with random sign inversion (the jack-knife method). In this method we apply the following steps to the time-stream data of each channel, independently. First, we subtract the time-integrated signal of the source from the entire time-stream data. Then we divide this source-subtracted time-stream data into blocks that contain one cycle of the telescope nodding, and randomly invert the sign of the signal contained in each block. The time-integration of this randomized set of data yields a single estimation of the source-subtracted intensity of each channel. We repeat this process for 100 times, and use the standard deviation as the estimation for the noise level at that channel. The channel-dependent error of the broadband spectra of VV 114 and IRC+10216 as shown in Fig. 1b and Fig. 4a, as well as the NEFDs shown in Fig. 4c, are determined using this method.